(Received 21 October 2025, Accepted 2 December 2025, Scheduled 3 February 2026)

Design and Optimization of an FPCB-Based Multi-Transmitter Single-Receiver Wireless Power Transfer System for Implantable Medical Devices

You Fu, Jianan Luo*, Xinguang Chen, and Dequan Jiang

College of Marine Electrical Engineering, Dalian Maritime University, Dalian, China

ABSTRACT: This study focuses on the design of a multi-transmitter single-receiver wireless power transfer (MTSR-WPT) system, particularly for implantable medical devices such as brain pacemakers. Conventional charging methods rely on invasive surgery or frequent battery replacement, posing significant challenges for patients. To address this issue, this work proposes an MTSR-WPT system based on a flexible printed circuit board (FPCB). The designed small-coil array topology leverages the mechanical flexibility of the FPCB to conform to complex biological surfaces, significantly enhancing two-dimensional omnidirectional anti-misalignment capability while reducing magnetic leakage during operation. To further compensate for misalignment between the transmitter and receiver, a backpropagation neural network optimized by the Seagull Optimization Algorithm (SOA-BP) is introduced for the receiver coil position prediction, combined with a fuzzy PID control strategy for dynamic output voltage regulation. Simulated and experimental results demonstrate that under a fixed load condition, the proposed system achieves stable energy transfer within a 120 mm charging area, maintaining an output power exceeding 1 W when the receiver coil is positioned at a height of 20 mm. Compared with traditional single-coil systems, the optimized multi-coil array exhibits superior performance in both misalignment tolerance and magnetic leakage suppression. These results verify the effectiveness of the proposed MTSR-WPT system and highlight its potential for implantable medical devices and other power electronic applications, providing a novel solution for achieving efficient and reliable wireless energy transfer.

1. INTRODUCTION

In recent years, driven by the growing demand for advanced medical technologies, a wide range of implantable medical devices (IMDs) have been actively developed. However, most existing IMDs still rely on electrochemical batteries or wired DC power supplies [1], which not only increase device volume but also necessitate secondary surgical procedures for battery replacement after depletion. The emergence of wireless power transfer (WPT) technology offers a safe, long-term, and convenient energy supply solution for implantable devices [2, 3].

WPT has been widely applied in various implantable medical systems, including implantable cardioverter defibrillators (ICDs) [4], deep brain stimulators (DBS) [5], cochlear implants (CIs) [6], and biomedical capsule endoscopy systems [7]. Its key advantage lies in eliminating frequent battery replacement surgeries while enabling stable long-term power delivery [8, 9]. Meanwhile, flexible printed circuit board (FPCB) technology, owing to its high flexibility and favorable biocompatibility, has been increasingly adopted in the design of implantable coils [10, 11], significantly enhancing structural freedom and adaptability.

Nevertheless, human body motion inevitably introduces spatial misalignment between the transmitting (Tx) and receiving (Rx) coils [12]. Conventional planar WPT systems require a strict coaxial alignment to achieve high coupling efficiency [13, 14]. Angular or lateral displacement leads to a sharp reduction in mutual inductance and coupling coefficient, resulting in degraded efficiency and potential system instability. Existing approaches to improve misalignment tolerance include enlarging coil dimensions [15], employing multi-coil array switching, or adopting multilayer stacked structures [16, 17]. However, these solutions often increase structural complexity and suffer from limited magnetic field uniformity, restricting their applicability in compact implantable systems.

To address these challenges, this paper proposes an FPCB-based multi-transmitter single-receiver wireless power transfer (MTSR-WPT) system combined with an intelligent adaptive control strategy to enhance robustness and power transfer stability. The proposed FPCB coil array exhibits high magnetic field uniformity and low magnetic leakage, effectively overcoming the limited energy concentration of conventional single-coil structures. In addition, a backpropagation neural network optimized by the Seagull Optimization Algorithm (SOA-BP), together with a fuzzy PID controller, is employed to enable adaptive regulation under dynamic misalignment and load variations. Finite-element simulations and experimental results demonstrate that the proposed system achieves superior transmission efficiency, misalignment tolerance, and electromagnetic safety performance.

The remainder of this paper is organized as follows. Section 2 presents the overall system architecture and the equivalent circuit model. Section 3 focuses on the optimization of

* Corresponding author: Jianan Luo (jnluo@dlmu.edu.cn).

coil geometric parameters and the design of a coupling mechanism suitable for implantable medical devices. Section 4 introduces the intelligent control strategy based on the SOA-BP neural network and fuzzy PID control. Experimental validation is provided in Section 5, and conclusions are drawn in Section 6.

2. CIRCUIT MODELING AND EFFICIENCY ANALYSIS

In this section, we develop a circuit model for the MTSR-WPT system and derives analytical expressions for the key parameters and system efficiency. A parametric analysis is conducted to identify the dominant factors affecting the power transfer performance, providing a theoretical basis for hardware design and coil optimization.

As illustrated in Figure 1, the proposed MTSR-WPT system employs an array Tx comprising seven self-decoupled, partially overlapping flexible FPCB coils integrated with ferrite, enabling conformal bending to accommodate practical deployment. The Rx consists of a single coil with identical material and geometrical parameters to the transmitting coils, also backed by ferrite. Within a circular charging region of 120 mm in diameter, a microcontroller unit (MCU) adaptively activates one to four transmitting coils in closest proximity to the receiver, while the remaining coils are maintained in an open-circuit state. As the receiver position varies, the MCU continuously estimates its location and reconfigures the active transmitter set to ensure stable power transfer. The corresponding localization algorithm and control strategy are detailed in subsequent sections.

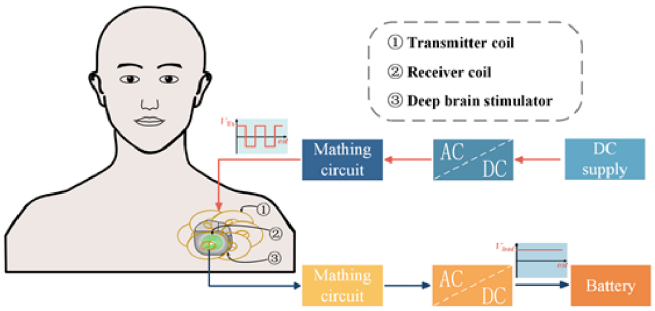

FIGURE 1. MTSR-WPT system for implantable medical devices.

Figure 2(a) illustrates the simplified equivalent circuit of the MTSR-WPT system under steady-state operation. To achieve stable power transfer over a wide range of positional variations, an LCC-S compensation network is employed at the transmitter side. In this topology, the series inductor and shunt capacitor establish an approximately constant-current characteristic, effectively suppressing transmitter current fluctuations induced by coupling variations and thereby maintaining a stable load-side output voltage. The receiver adopts a series-compensated resonant structure, featuring a compact topology and ease of integration. According to the standard design principles of LCC-S resonant converters [18], ω should satisfy:

$$\omega = \frac{1}{\sqrt{L_{lcc}C_{lcc}}} = \frac{1}{\sqrt{L_{Rx}C_s}} = \frac{1}{\sqrt{(L_{Tx,i} - L_{lcc})\,C_{Tx,i}}} \tag{1}$$

The system employs a full-bridge inverter topology, as shown in Figure 2(b), to convert the DC voltage V_{DC} into a high-frequency square-wave driving voltage V_{SW}. Considering the presence of multiple activation modes under actual operating conditions, V_{SW} can be equivalently represented as either an AC voltage source or an open circuit, depending on the operating state. When operating in the open-circuit mode, both V_{SW} and the fundamental component of the high-frequency current I_{SW} can be approximated as zero. In contrast, when V_{SW} functions as an AC voltage source, the power transfer characteristics of the system can be analyzed according to the following circuit model. To simulate different activation combinations, let the activation set be defined as $\mathcal{A} \subseteq \{\text{No. } 1, 2, 3, 4, 5, 6, 7\}$, where the number of active transmitter units is denoted as $N = |\mathcal{A}|$. Denote the parasitic resistance and the equivalent load resistance of the receiving coil as R_{Rx} and R_L, respectively. According to [19], α is the coefficient for calculating the equivalent AC resistance, and the equivalent impedance of the receiving coil Z_{Rx} can be expressed as:

$$Z_{Rx} = R_{Rx} + j\omega L_{Rx} + \frac{1}{j\omega C_s} + \alpha R_L, \quad \alpha = \frac{8}{\pi^2} \tag{2}$$

The impedance at the receiving end can be reflected to the transmitting end through the mutual inductive coupling, and the corresponding equivalent reflected impedance can be expressed as:

$$Z_{ref,i} = \frac{(j\omega M_i)^2}{Z_{Rx}}, \quad \forall i \in \mathcal{A} \tag{3}$$

Here, M_i denotes the mutual inductance between the ith activated transmitting coil and the receiving coil. This expression indicates that the load at the receiving end not only determines the power transfer path but also directly affects the input characteristics of each transmitting unit through mutual coupling.

Furthermore, each activated transmitting unit possesses independent parameters $R_{Tx,i}$, $L_{Tx,i}$, and $C_{Tx,i}$, while the compensation components L_{lcc} and C_{lcc} are shared among all transmitting units. In this case, the receiving-end impedance Z_{Rx} is reflected to each transmitting branch via the mutual inductance M_i and, together with the impedance of the transmitting branch, forms the total primary-branch impedance:

$$Z_{main,i} = R_{Tx,i} + j\omega L_{Tx,i} + \frac{1}{j\omega C_{Tx,i}} + Z_{ref,i} \tag{4}$$

All activated transmitting units are connected in parallel with the common compensation network composed of L_{lcc} and C_{lcc}. Therefore, they can be combined to form the total impedance at the transmitting side, which can be expressed as:

$$Z_{Tx,i} = j\omega L_{lcc} + \left(\frac{1}{Z_{main,i}} + j\omega C_{lcc}\right)^{-1} \tag{5}$$

On this basis, when the inverter supplies an AC driving voltage V_{SW} to the system, the input current flowing into the ith transmitting branch can be expressed by Equation (6), while the

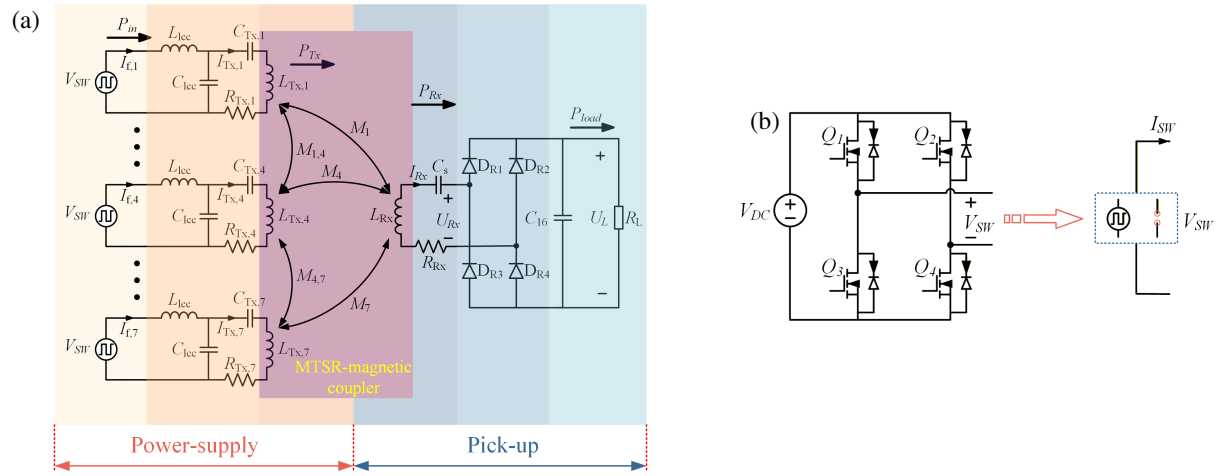

FIGURE 2. Schematic overview of the proposed power electronics system. (a) LCC-S equivalent circuit, (b) dual-mode power supply.

actual current through the transmitting coil is given by Equation (7):

$$I_{f,i} = \frac{V_{SW}}{Z_{Tx,i}} \tag{6}$$

$$I_{Tx,i} = \frac{V_{SW} - j\omega L_{lcc} I_{f,i}}{Z_{main,i}} \tag{7}$$

Under the multi-channel excitation of the transmitter array, the fundamental induced voltages at the receiver from the individual transmitting coils are linearly superimposed. Consequently, the net induced response can be expressed as the phasor summation of the magnetic coupling contributions. For analytical simplicity, the coupling of the MTSR-WPT system is equivalently characterized by defining an effective mutual inductance M_{eq} for the active set $\mathcal{A}$ based on the individual mutual inductance M_i:

$$M_{eq}(\mathcal{A}) = \sum_{i\in\mathcal{A}} M_i e^{j\phi_i} \tag{8}$$

where ϕ_i denotes the complex phase of the ith transmission path arriving at the Rx. The magnitude and phase of the equivalent mutual inductance M_{eq} represent the effective coupling strength and phase characteristics of the Tx array, respectively. Based on the above definition of the equivalent mutual inductance, the current at the Rx can be expressed as:

$$I_{Rx} = \frac{j\omega M_{eq}(\mathcal{A})}{Z_{Rx}} \sum_{i\in\mathcal{A}} I_{Tx,i} \tag{9}$$

By neglecting minor losses such as core loss and switching loss, and according to the principle of energy conservation, the total input active power of the system is equal to the sum of the copper losses in all transmitting branches, the active power dissipation in the receiving circuit, and the output power delivered to the load:

$$P_{in} = \sum_{i\in\mathcal{A}} |I_{Tx,i}|^2 R_{Tx,i} + |I_{Rx}|^2 R_{Rx} + P_{load} \tag{10}$$

The output power at the load can be further expressed as:

$$P_{load} = |I_{Rx}|^2 \alpha R_L \tag{11}$$

The overall system efficiency is defined as the ratio of the output power delivered to the load to the total input power of the system. Based on this definition, the efficiency expression of the MTSR-WPT system can be derived as follows:

$$\eta_{multi} = \frac{P_{load}}{P_{in}} = \left(1 + \frac{\sum_{i\in\mathcal{A}} |I_{Tx,i}|^2 R_{Tx,i}}{|I_{Rx}|^2 \alpha R_L} + \frac{R_{Rx}}{\alpha R_L}\right)^{-1} \tag{12}$$

Since the efficiency expression simultaneously involves both transmitter and receiver currents, it is not conducive to an intuitive analysis of the MTSR-WPT system efficiency. To further simplify the expression, the receiver current relation given in Equation (9) can be substituted into the efficiency definition in Equation (12), yielding:

$$\eta_{multi} = \left(1 + \frac{|Z_{Rx}|^2}{\omega^2 |M_{eq}|^2 \alpha R_L} \frac{\sum_{i\in\mathcal{A}} |I_{Tx,i}|^2 R_{Tx,i}}{\left|\sum_{i\in\mathcal{A}} I_{Tx,i}\right|^2} + \frac{R_{Rx}}{\alpha R_L}\right)^{-1} \tag{13}$$

When the transmitter currents are assumed to have identical amplitudes and phases, the current set can be expressed as:

$$\sum_{i\in\mathcal{A}} I_{Tx,i} = N I_{Tx} \tag{14}$$

At this stage, the efficiency of the MTSR-WPT system can be expressed by Equation (15):

$$\eta_{multi} \simeq \left[1 + \frac{\left(\sum_{i\in\mathcal{A}} R_{Tx,i}\right) \frac{|Z_{Rx}|^2}{N\omega^2 |M_{eq}|^2} + R_{Rx}}{\alpha R_L}\right]^{-1} \tag{15}$$

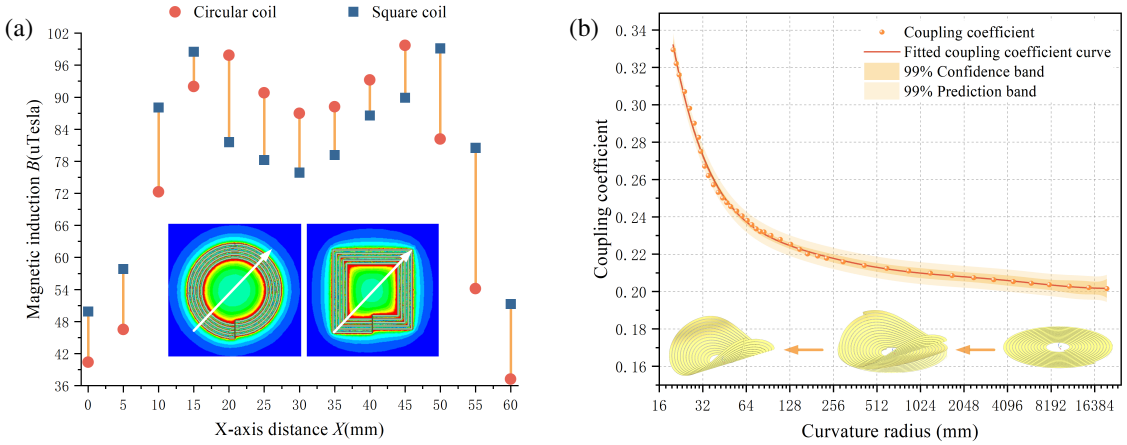

FIGURE 3. Magnetic field characteristics and coupling performance of FPCB coils. (a) Magnetic induction profiles of circular and square coils along the X-axis. (b) Coupling coefficient variation of FPCB coils under different curvature radii.

When the amplitudes or phases of the Tx currents are non-identical, the system efficiency should be evaluated using Equation (13). In practical operation, however, the current ratios among the transmitting coils remain nearly constant, and thus the efficiency can be primarily characterized by the ratio between the equivalent transmitter resistance and the effective mutual inductance. As indicated by Equation (12), the efficiency is jointly determined by the Tx and Rx currents, implying that activating more coils does not necessarily improve efficiency. Although multi-coil excitation enhances magnetic coupling, it also increases copper loss, introducing additional dissipation. Accordingly, this relationship reveals the fundamental coupling-loss tradeoff in system efficiency: at any receiver position, the Tx coil combination with the lowest ratio of equivalent loss to mutual inductance should be preferred, rather than simply maximizing the total mutual inductance or the number of active coils. Consequently, the system efficiency is mainly governed by the relative proportion of Tx copper loss and effective load impedance. Based on this insight, Section 3 focuses on optimizing the coil geometry to reduce losses and enhance power transfer performance in implantable medical devices.

3. STRUCTURAL PARAMETER OPTIMIZATION AND PERFORMANCE ENHANCEMENT OF COILS

As the key component responsible for energy coupling in WPT systems, the coil's geometric configuration and electrical parameters directly affect the transmission efficiency and operational stability of the system. At present, research on coupling coils primarily focuses on the optimization of coil topology and structural parameters [20, 21]. In response to the stringent requirements for miniaturization and high efficiency in implantable medical devices such as brain pacemakers, this study systematically optimizes the design of the transmitting coil, clarifying the objectives and methodology of coil optimization.

3.1. Geometric Design and Electromagnetic Characteristics of Coils

Based on their spatial configurations, planar spiral coils can be categorized into three-dimensional spiral coils and two-dimensional planar coils. Considering the stringent constraints on size, thickness, and packaging space in implantable medical devices, this study focuses on two-dimensional planar spiral coils and compares two representative geometries: circular and square coils. Figure 3(a) illustrates the magnetic flux density distribution along the diagonal direction and the corresponding three-dimensional magnetic field maps. The results indicate that, under identical characteristic dimensions and turn numbers, the circular coil exhibits higher overall magnetic flux density with a more uniform distribution and reduced fluctuation compared to the square coil. This advantage is mainly attributed to the higher geometric symmetry of the circular structure, which mitigates the magnetic field distortion and leakage at corner regions, thereby achieving higher effective coupling efficiency and more stable power transfer under the same excitation conditions. Consequently, circular coils are more suitable for wireless power transfer systems requiring high magnetic field uniformity [22, 23].

To further investigate the effect of structural deformation on the coupling performance, the magnetic coupling characteristics between FPCB-based transmitting and receiving coils with different curvature radii are analyzed through simulation, as shown in Figure 3(b). The simulation data are fitted using a polynomial model with a coefficient of determination of $R^2 = 0.99755$ indicating excellent agreement. The 99% confidence band and prediction band are also presented to validate the reliability of the model under varying curvature conditions. The results demonstrate that the coupling coefficient increases significantly as the curvature radius decreases, suggesting that moderate bending enhances the magnetic field concentration and improves power transfer efficiency, while substantially improving the mechanical flexibility and deformation adaptability of the coupling structure [24].

3.2. Optimization Objectives and Mathematical Modeling

After determining the coil geometry and material selection, the subsequent optimization objective is to improve the overall system performance, with particular emphasis on transmission efficiency and magnetic leakage control. Based on the previously derived efficiency expression for the seven-coil array, the efficiency at the resonant condition can be expressed as follows:

$$Z_{Rx} = R_{Rx} + \alpha R_L, \quad R_{Rx} = \frac{\omega L_{Rx}}{Q_{Rx}} \tag{16}$$

Here, the total impedance of the receiver, Z_{Rx}, is purely resistive at the resonance point, and Q_{Rx} denotes the quality factor of the receiver coil [25]. Further, let:

$$Q_{Tx,eq} = \frac{\omega L_{Tx,eq}}{\sum_{i\in\mathcal{A}} R_{Tx,i}}, \quad L_{Tx,eq} = \sum_{i\in\mathcal{A}} L_{Tx,i} \tag{17}$$

Since all Tx units share identical materials and geometrical structures, their equivalent self-inductances are approximately uniform. For analytical convenience, they can be represented by a single equivalent self-inductance $L_{Tx,eq}$, with a corresponding quality factor $Q_{Tx,eq}$. Based on this, the mutual coupling between each Tx unit and the Rx, denoted as k_i, as well as the effective coupling coefficient k_{eq}, can be further defined as:

$$k_i = \frac{M_i}{\sqrt{L_{Tx,i} L_{Rx}}} \tag{18}$$

$$k_{eq}^2 = \frac{|M_{eq}|^2}{L_{Tx,eq} L_{Rx}} = \frac{\left|\sum_{i\in\mathcal{A}} k_i \sqrt{L_{Tx,i}} e^{j\phi_i}\right|^2}{L_{Tx,eq}} \tag{19}$$

When only a single transmitting unit is activated, substituting Equations (16)–(19) into the previously derived seven-coil array efficiency expression Equation (15) yields:

$$\eta_{multi} = \left[1 + \frac{1}{\alpha}\left(\frac{1}{Q_{Tx,eq} Q_{Rx} k_{eq}^2} \frac{|Z_{Rx}|^2}{R_L R_{Rx}} + \frac{R_{Rx}}{R_L}\right)\right]^{-1} \tag{20}$$

Clearly, the system efficiency increases significantly with the growth of $Q_{Tx,eq} Q_{Rx} k_{eq}^2$. Therefore, maximizing $Q_{Tx,eq} Q_{Rx} k_{eq}^2$ constitutes the central objective of coil parameter optimization in this section. In the parameter optimization process of this study, the objective function is defined as the strong coupling coefficient k_s:

$$k_s = Q_{Tx,eq} Q_{Rx} k_{eq}^2 \tag{21}$$

Based on the above mathematical modeling, the optimization target for the coils has been identified as the strong coupling coefficient k_s. In the following section, the focus will be on enhancing the array's equivalent coupling capability and quality factor through the optimization of geometric parameters, such as coil radius, spacing, number of turns, and conductor width, thereby achieving the goal of maximizing k_s.

3.3. Influence of Key Geometric Parameters on Coupling Performance

In the FPCB planar coil design, electromagnetic characteristics are mainly determined by geometric parameters, including conductor thickness, number of turns, trace width, and inter-turn spacing. To evaluate power transfer performance for biomedical applications, multiple coil geometries are modeled and analyzed using finite-element simulations at 100 kHz. This frequency is commonly used in implantable wireless power transfer systems, providing a balance among efficiency, tissue penetration, and specific absorption rate (SAR) safety [26]. A representative coil structure is shown in Figure 4.

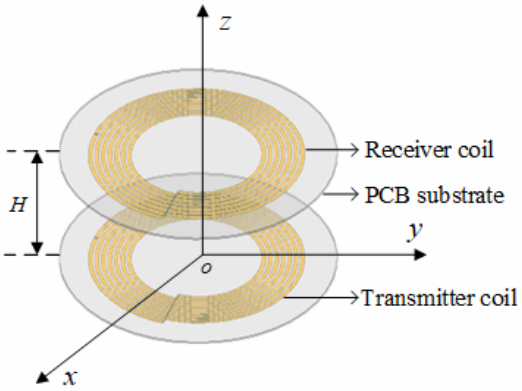

FIGURE 4. Single-coil three-dimensional model of an array transmitter.

Common copper thicknesses for the FPCB coils are 0.018 mm and 0.035 mm. To investigate the effects of conductor thickness and turn-to-turn spacing on coil performance, simulations were conducted under the conditions of an outer diameter of 6 cm, a trace width of 1 mm, and 6 turns. The results (Table 1 and Figure 5) indicate that increasing the thickness from 0.018 mm to 0.035 mm results in nearly unchanged self-inductance and mutual inductance, while the resistance decreases significantly, demonstrating that a larger copper thickness effectively reduces ohmic losses. Meanwhile, for the same turn-to-turn spacing, the strong coupling coefficient of the 0.035 mm thick coil is noticeably higher, and this advantage becomes more pronounced as the spacing decreases. Considering both the simulation outcomes and the FPCB manufacturing limit (maximum thickness of 1 oz, i.e., 0.035 mm), a copper thickness of 0.035 mm was selected as

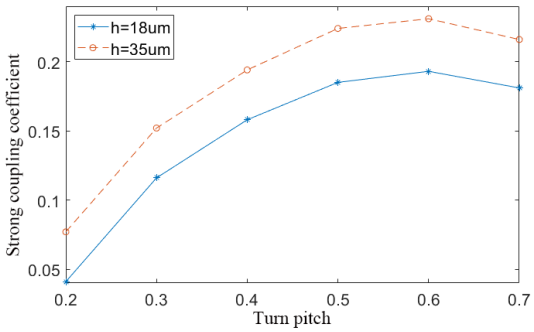

FIGURE 5. Strong coupling coefficient of coils with different thicknesses.

TABLE 1. Self-inductance, mutual inductance, and resistance of coils with different thicknesses.

Coil Thickness (mm)	Turn Pitch (mm)	Self-inductance (μH)	Mutual Inductance (μH)	Resistance (mΩ)
0.018	0.2	3.524	1.329	857.14
	0.4	2.182	0.937	387.45
	0.6	1.381	0.604	221.9
0.035	0.2	3.513	1.325	477.38
	0.4	2.181	0.93	210.94
	0.6	1.378	0.597	124.08

the final coil thickness to balance manufacturing feasibility and optimal efficiency.

Building upon the thickness optimization, the geometric ratio parameters of the coil were further analyzed. Since planar spiral coils are wound from a single conductor, altering the turn-to-turn spacing alone while keeping the trace width constant would change the coil curvature and consequently affect its electromagnetic characteristics. To maintain geometric consistency, a width-to-spacing ratio (the ratio of trace width to turn-to-turn spacing) was introduced. When this ratio is fixed, both the spacing and trace width are adjusted proportionally to preserve a constant curvature. This approach ensures comparability across coils with different structural parameters.

Further analysis indicates that the width-to-spacing ratio, trace width, and number of turns are highly coupled: a smaller width-to-spacing ratio allows for more turns, whereas a larger ratio limits the number of turns. Together, these three parameters nonlinearly affect the coupling coefficient and transmission efficiency. To determine the optimal parameter combination, a multi-parameter cooperative optimization strategy was employed. The coils were divided into five groups, A-E, according to their width-to-spacing ratios (ranging from 3 to 7), and each group was further subdivided by the number of turns (6–14 turns). For example, in Group C (width-to-spacing ratio of 5), subgroup C9 represents a 9-turn configuration. Using the strong coupling coefficient as the optimization objective, the trace width was scanned within each subgroup to determine the optimal solution, and a global optimum was subsequently obtained through inter-group comparison.

Taking Group C as an example, for a coil with an outer diameter of 6 cm and an inter-turn spacing of 0.45 mm, the trace width is 2.25 mm, and the inner diameter is 11.4 mm. Due to physical constraints, the inter-turn spacing was scanned within the range of 0.2–0.45 mm with a step size of 0.05 mm, resulting in the geometric correspondences shown in Table 2. Figure 6(a) depicts the variation of the strong coupling coefficient and transmission efficiency of the C9 coil as a function of the inter-turn spacing, indicating that the efficiency reaches its peak at 0.41 mm. Figure 6(b) shows that the global optimum for Group C occurs with the 14-turn coil, which achieves a transmission efficiency of 5.87%. Further simulation results (Table 3) reveal that reducing the width-to-spacing ratio enhances both the strong coupling coefficient and the transmission efficiency. Among all groups, Group E (width-to-spacing ratio of 7, 14 turns) exhibits the best performance, with an efficiency of 6.34%.

TABLE 2. The correspondence between coil line width, inner diameter, and turn spacing.

Turn Pitch (mm)	0.2	0.25	0.3	0.35	0.4	0.45
Trace Width (mm)	1	1.25	1.5	1.75	2	2.25
Inner Diameter (mm)	38.4	33	27.6	22.2	16.8	11.4

TABLE 3. Optimal coil simulation results.

Optimal Parameters	A	B	C	D	E
Number of Turns	9	14	14	13	14
Turn Pitch (mm)	0.6	0.32	0.28	0.27	0.21
Coupling Coefficient	0.232	0.245	0.265	0.28	0.29
Transmission Efficiency (%)	5.22	5.46	5.87	6.17	6.34

Based on the simulation results from multiple groups, it can be concluded that increasing the copper thickness effectively reduces resistance and enhances the strong coupling coefficient, while a proper selection of the width-to-spacing ratio and number of turns can further optimize the magnetic coupling and transmission efficiency. Considering the FPCB manufacturing limits and coil geometric constraints, the optimal geometric parameters determined in this study are summarized in Table 4: copper thickness of 0.035 mm, outer diameter of 6 cm, turn-to-turn spacing of 0.21 mm, trace width of 1.47 mm, 14 turns, and an inner diameter of 12.96 mm, yielding the best overall performance.

TABLE 4. Optimal parameters of the coil.

Thickness (mm)	Outer Diameter (cm)	Turn Pitch (mm)	Trace Width (mm)	Number of Turns	Inner Diameter (mm)
0.035	6	0.21	1.47	14	12.96

4. MULTI-TRANSMITTER ARRAY FOR WIRELESS POWER TRANSFER WITH MISALIGNMENT TOLERANCE

In wireless power transfer for implantable brain pacemakers, physiological body motion can cause spatial misalignment between the transmitting and receiving coils, leading to reduced magnetic coupling, increased leakage inductance, and a significant drop in transmission efficiency [27–29]. To address this issue, a MTSR-WPT system is developed based on the optimized single-coil design and compared with a single-coil sys-

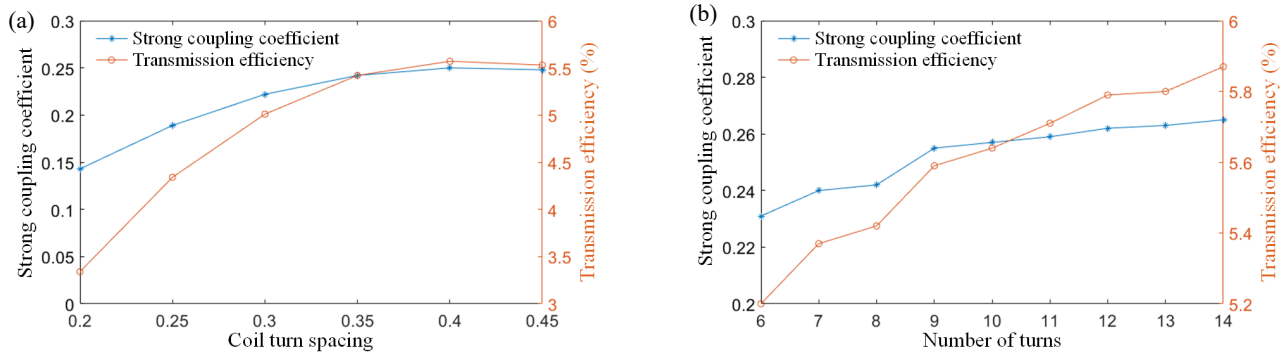

FIGURE 6. Influence of geometric parameters on coupling coefficient and transmission efficiency. (a) Relationship between coupling coefficient, transmission efficiency, and inter-turn spacing. (b) Relationship between coupling coefficient, transmission efficiency, and number of turns under different inter-turn spacings.

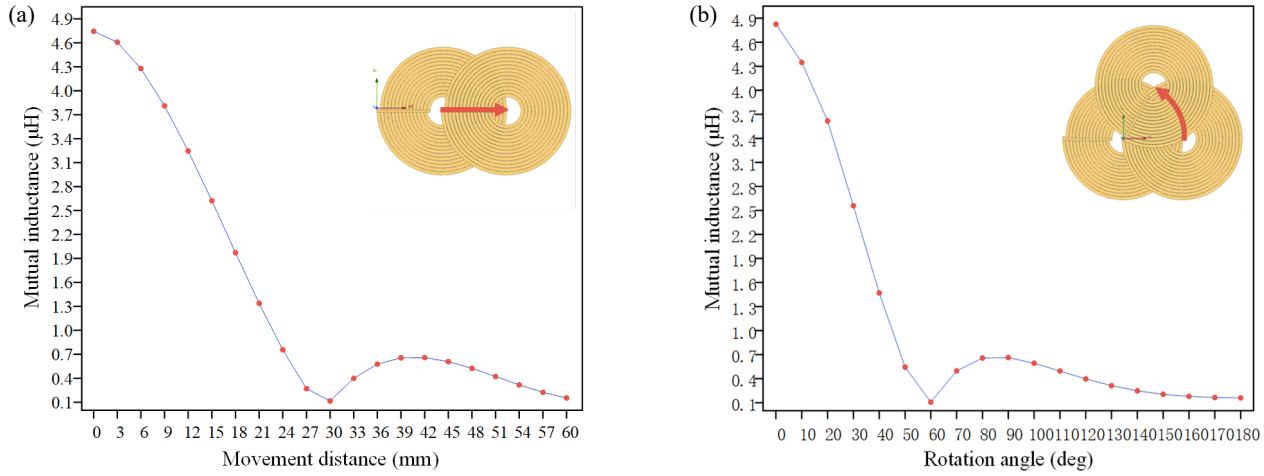

FIGURE 7. Relationship diagrams of coil motion parameters and mutual inductance changes. (a) Diagram of the relationship between the lateral movement of the coil and the corresponding change in mutual inductance. (b) Diagram of the relationship between coil rotation angle and corresponding mutual inductance changes.

tem of equal area to evaluate improvements in misalignment tolerance and magnetic field uniformity. In addition, a seagull-optimized BP neural network combined with a fuzzy PID control algorithm is employed to enable receiver position identification and adaptive output voltage regulation. The effectiveness of the proposed approach is validated in the subsequent experimental section.

4.1. Array Transmitter Modeling

In a multi-transmitter array, each transmitting element not only couples with the receiving coil but also exhibits cross-coupling with adjacent coils. Although such coupling may locally enhance the magnetic field, it also leads to power dispersion and additional losses. To balance the effective coupling and cross-coupling, the effects of the coil spacing and rotational angle are investigated through electromagnetic simulations. The results show that the mutual inductance is maximized under coaxial alignment and decreases with increasing lateral misalignment, following a "decrease-increase-decrease" trend [30]. When the center-to-center distance is approximately 30 mm, cross-coupling is significantly suppressed, and the magnetic field distribution becomes most uniform, as shown in Figure 7(a). Furthermore, a third coil is introduced to examine the effect of rotational angle on mutual inductance, as illustrated in Figure 7(b). The results indicate that a rotation angle of 60° yields a local minimum in cross-coupling, demonstrating the effectiveness of this configuration in reducing the electromagnetic interference between coils.

Based on the aforementioned analysis, a seven-coil circular array structure was adopted (Figure 8). This configuration consists of seven identical planar spiral coils, with one positioned at the center and six uniformly distributed around the periphery at 60° intervals to form a symmetrical layout. The center-to-center distance between the outer coils and the central coil is 60 mm, resulting in an overall array outer diameter of approximately 120 mm. This layout effectively reduces cross-coupling and far-field leakage while maintaining a compact structure. Furthermore, each transmitting unit is equipped with independent excitation control, enabling adaptive adjustment of the excitation combination according to the receiver coil position. This allows for the dynamic optimization of magnetic field distribution and provides a structural foundation for subsequent excitation strategies and control algorithms.

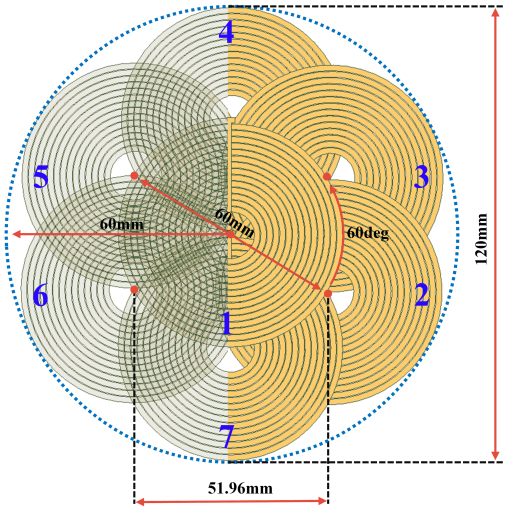

FIGURE 8. Overhead view of the overlapping array transmitter.

4.2. Adaptive Excitation Strategy Based on Spatial Partitioning

After optimizing the geometric parameters of transmitting coils, it is still necessary to consider the potential two-dimensional translational offsets of the receiving coil during practical operation. Relying solely on a static topological design is insufficient to simultaneously achieve high energy transfer efficiency and low magnetic leakage across all receiver positions. Therefore, based on Equation (15) in Section 2, the ratio of the transmitting-end equivalent mutual inductance to the equivalent loss is defined as the Efficiency-Dominant Ratio (EDR):

$$\Lambda(\mathcal{A}) = \frac{\sum_{i\in\mathcal{A}} R_{Tx,i}}{N\omega^2 \left|M_{eq}\right|^2} \tag{22}$$

This ratio is used to characterize the overall trade-off between energy coupling strength and losses. At each offset position, the optimal combination of transmitting units is selected by calculating the EDR to achieve a balance between efficiency and safety [31]. Specifically, parametric simulations of the magnetic flux density distribution at different positions of the receiving coil within the same plane were conducted, leading to the proposal and validation of a subregion activation strategy that prioritizes leakage suppression while also considering the energy transfer efficiency (as shown in Figure 9). The simulation results in Section 4.5 demonstrate that this strategy effectively minimizes unnecessary energy dispersion and significantly reduces far-field magnetic leakage, while maintaining stable energy transfer. Using the coordinate origin O as a reference, the working plane is divided into five regions by concentric circles with radii of 7.5 mm, 15 mm, and 30 mm. The corresponding local excitation rules are described as follows:

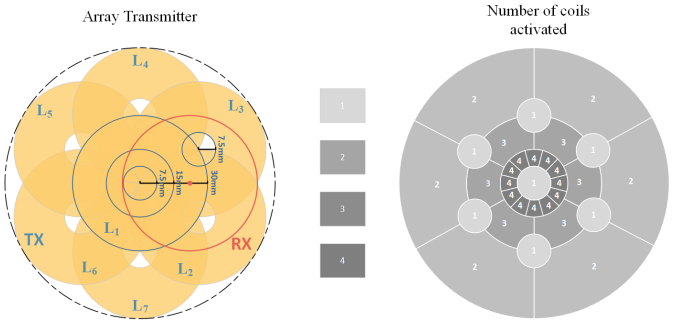

FIGURE 9. Correspondence between the receiver coil position and the excitation scheme of the transmitting coils.

a. Region 1 (radius $\leq$ 7.5 mm): When the receiving coil exhibits minimal offset, and the magnetic field is highly uniform, only the central coil (coil 1) is activated to achieve efficient, localized energy transfer.

b. Region 2 (7.5–15 mm annular band): This band is divided into six 60° sector regions. When the receiving coil is located at a sector boundary, adjacent coils are sequentially activated in a counterclockwise direction. If the receiving coil lies on the outer boundary of the annular band (e.g., x-axis offset of 10 mm), it is recommended to primarily activate coils 1, 2, 3, and 4 to balance coupling strength and magnetic leakage control.

c. Region 3 (15–30 mm annular band): Compared to Region 2, the sector divisions in this region are rotated by 30° in angle. The optimal strategy for this region is to activate three adjacent transmitting units (e.g., coils 1, 2, and 3 when the x-axis offset is 25 mm) to enhance local coupling and suppress far-field leakage.

d. Region 4 (30–60 mm annular band): The division rules are the same as those of Region 2. However, for larger offset distances, it is recommended to activate two adjacent coils (e.g., coils 2 and 3 when the x-axis offset is 45 mm) to balance transfer efficiency and magnetic leakage control.

e. Region 5 (within a 7.5 mm radius around the center of each transmitting sub-coil): If the receiving coil is located near the center of any individual transmitting coil (e.g., y-axis offset of 31 mm falling within the coverage of coil 4), only the corresponding sub-coil is activated to satisfy offset tolerance and safety requirements.

4.3. Receiver Coil Position Prediction

This subsection describes how the position of the receiving coil can be estimated by measuring its output voltage. Based on the derivations in Section 2, the mutual inductance between the two coils directly affects several parameters in the receiver circuit. Therefore, by measuring relevant parameters in the receiver circuit to obtain the mutual inductance and subsequently applying Neumann's formula [32], the relative position of the receiving coil can be determined. Accordingly, the main tasks of this subsection include establishing the relationship between mutual inductance and the receiver position, as well as addressing the nonlinear issues inherent in the corresponding equations.

According to Figure 2 and Equation (9), when phase control is applied to ensure that the total phase arriving at the receiver point from each transmitting path is consistent — i.e., when the equivalent mutual inductance or induced voltage increases linearly with the number of activated units — its M_{eq} can be

expressed as follows:

$$M_{\text{eq}}(\mathcal{A}) = \frac{Z_{Rx}}{j\omega}\frac{I_{Rx}}{\sum_{i\in\mathcal{A}} I_{Tx,i}} = \frac{U_{Rx}}{j\omega\sum_{i\in\mathcal{A}} I_{Tx,i}} \tag{23}$$

where $U_{Rx} = Z_{Rx}I_{Rx}$ represents the alternating voltage at the receiver end, as shown in the circuit diagram. From this, it can be inferred that, when the receiver impedance Z_{Rx} is known, under the condition of equal amplitude in-phase excitation, the equivalent mutual inductance M_{eq} can be calculated by measuring the input current of each transmitting unit and the fundamental component of the output voltage at the receiver end, as per Equation (23).

To more accurately predict the spatial position of the receiving coil, a three-dimensional Cartesian coordinate system is established for this model. The center of the equivalent large transmitting coil C_1 (Coil A) is set as the coordinate origin (0, 0, 0), with a radius of r_1. The center of the receiving coil C_2 (Coil B) is designated as the coordinate (x, y, z), with a radius of r_2. The differential segment vectors of C_1 and C_2 are denoted as dl_1 and dl_2, respectively, as shown in Figure 10. The coordinates (x, y, z) of the receiving coil are the unknown variables to be solved, and can be inferred by measuring the mutual inductance between multiple transmitting coils and the receiving coil to determine the relative displacement of the receiving coil with respect to the transmitting coils.

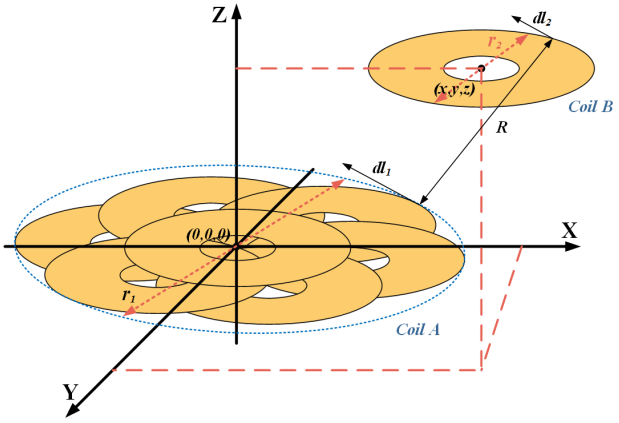

FIGURE 10. Geometric model of coil in three-dimensional coordinate system.

The position vectors r_1 and r_2 of coils C_1 and C_2 in Figure 10 can be expressed as Equation (24).

$$\begin{cases} r_1(\phi_1) = (r_1\cos\phi_1, r_1\sin\phi_1, 0) \\ r_2(\phi_2) = (x + r_2\cos\phi_2, y + r_2\sin\phi_2, z) \end{cases} \tag{24}$$

The differential vectors dl_1 and dl_2 of C_1 and C_2 can be expressed as Equation (25).

$$\begin{cases} dl_1 = \frac{dr_1}{d\phi_1}d\phi_1 = (-r_1\sin\phi_1, r_1\cos\phi_1, 0)d\phi_1 \\ dl_2 = \frac{dr_2}{d\phi_2}d\phi_2 = (-r_2\sin\phi_2, r_2\cos\phi_2, 0)d\phi_2 \end{cases} \tag{25}$$

According to the Neumann formula, the mutual inductance between C_1 and C_2 can be expressed as Equation (26), where μ_0 is the permeability of free space.

$$M_{\text{eq}} = \frac{\mu_0}{4\pi}\oint_{C_1}\oint_{C_2}\frac{dl_1 dl_2}{R} \tag{26}$$

The spatial distance R between the two differential segments dl_1 and dl_2 is given by Equation (27). Substituting Equations (25) and (26) into (27) yields the mutual inductance of the coils as shown in Equation (28).

$$R = \sqrt{\begin{array}{l}(r_1\cos\phi_1 - (x + r_2\cos\phi_2))^2 \\ +(r_1\sin\phi_1 - (y + r_2\sin\phi_2))^2 + (0 - z)^2\end{array}} \tag{27}$$

$$M_{\text{eq}} = \frac{\mu_0 r_1 r_2}{4\pi}\int_0^{2\pi}\int_0^{2\pi} \frac{\cos(\phi_1 - \phi_2)}{\sqrt{\begin{array}{l}(r_1\cos\phi_1 - x - r_2\cos\phi_2)^2 \\ +(r_1\sin\phi_1 - y - r_2\sin\phi_2)^2 + z^2\end{array}}} d\phi_1 d\phi_2 \tag{28}$$

From Equation (28), it can be observed that the number of transmitting units activated by the array transmitter varies with the receiver's position, and the mutual inductance between each transmitting unit and the receiving coil also differs, exhibiting complex nonlinear characteristics. Since such nonlinear functions are difficult to derive an explicit analytical expression for using conventional mathematical methods, the relationship between mutual inductance and the receiver's position is represented as shown in Equation (29):

$$M_{eq} = F(x, y, z) \tag{29}$$

To address the highly nonlinear coil positioning problem described above, this paper introduces a BP neural network based on the SOA for precise prediction of the receiving coil's position. SOA performs global optimization by simulating the dynamic behavior of seagull flocks during migration. Its optimization mechanism mainly includes three constraints: avoiding collisions between individuals, migrating towards the optimal neighboring direction, and converging towards the global optimum solution region. This migration and update process is represented by the mathematical model shown in Equation (30):

$$\overline{C} = \overline{X} * A, A = f_c - \frac{tf_c}{Max_{iteration}}, D_s = \left|C_s + M_s\right| \tag{30}$$

In implementation, the SOA is embedded into a BP neural network to optimize the initial weights and biases, thereby improving convergence speed and prediction accuracy. The input vector is defined as $x_i = M_i$ $(i = 1 \sim 7)$, and the training data are obtained from the grid-labeled coupling platform, as shown in Figure 15. The charging area covers 120 mm × 120 mm, within which two sampling points are randomly selected in each grid cell, yielding a total of 128 data sets. Among them, 88 samples are used for training and 40 for testing. At each sampling point, the receiver voltage, input current, and output power are measured under identical system parameters, and the grid coordinates of the platform are used as position labels. The training objective is to minimize the error between

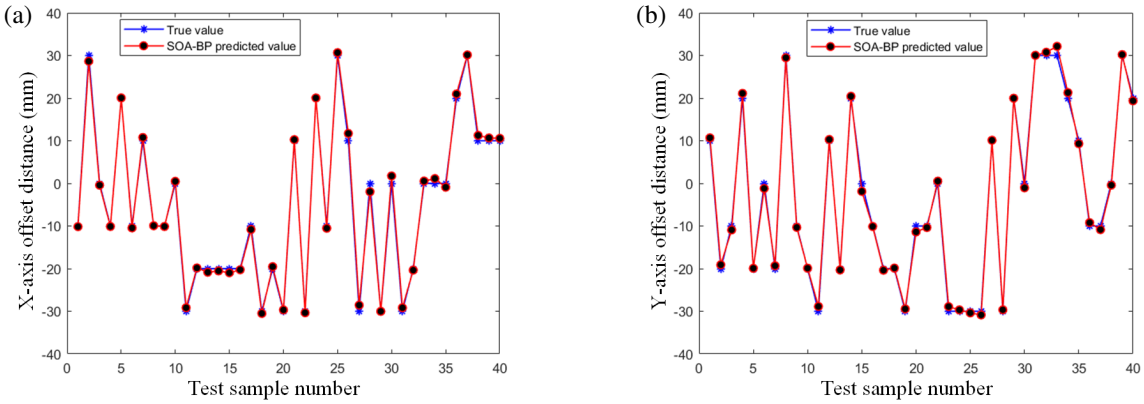

FIGURE 11. Comparison between predicted and actual values of SOA-BP neural network.

the predicted and actual coordinates, with a standard deviation constraint incorporated into the loss function as follows:

$$\sigma = \sqrt{\frac{1}{N}\sum_{i=1}^{N}\left(x_i - \frac{1}{N}\sum_{i=1}^{N}x_i\right)^2} \tag{31}$$

The prediction results are shown in Figure 11, where the SOA-BP model exhibits close agreement with the measured values, indicating high fitting accuracy. To further evaluate the spatial generalization capability, the Euclidean distance between the predicted points and the ground-truth positions is calculated, and a three-dimensional error surface is plotted, as shown in Figure 12.

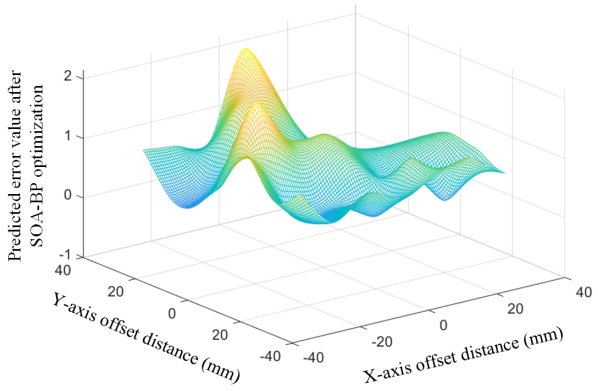

FIGURE 12. Prediction errors before and after SOA optimization.

The results indicate that the error distribution is concentrated and smooth, demonstrating stable prediction performance of the SOA-BP model over the entire operating region. Quantitative analysis shows that SOA optimization significantly reduces prediction dispersion in all directions: the standard deviation along the x-axis decreases from 2.564 mm to 0.535 mm, along the y-axis from 2.006 mm to 0.671 mm, and under simultaneous x-y offsets from 1.883 mm to 0.441 mm. Compared with the conventional BP neural network reported in [33], the SOA-BP model achieves superior convergence speed and prediction accuracy, thereby validating the effectiveness and robustness of the proposed position prediction method.

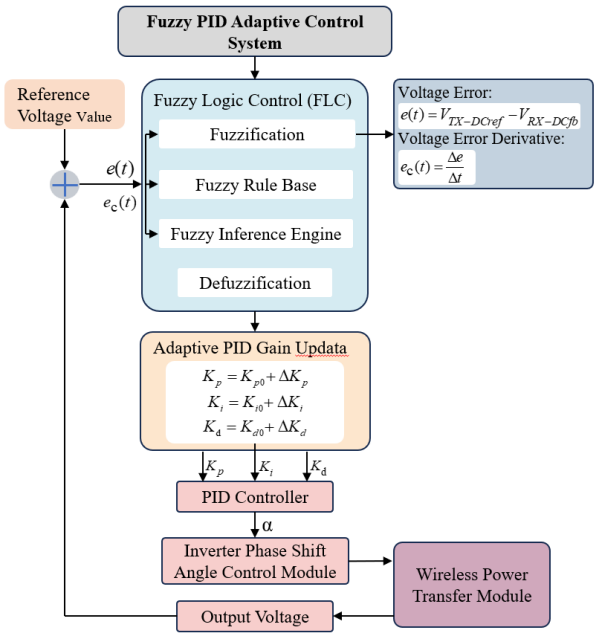

FIGURE 13. Flowchart of the fuzzy PID adaptive control system.

4.4. Fuzzy PID Adaptive Control Strategy

To mitigate output voltage fluctuations under dynamic coupling conditions, this paper proposes a fuzzy logic-based adaptive PID controller that enables rapid compensation for nonlinear disturbances while ensuring stable steady-state regulation [34]. The fuzzy PID control scheme consists of five stages: error acquisition, fuzzification, rule-based inference, defuzzification, and adaptive parameter updating. The overall architecture of the control system is illustrated in Figure 13. The controller takes the output voltage error $e(t)$ and its rate of change $e_c(t)$ as inputs, while the phase-shift angle α of the primary-side inverter serves as the control output. The PID gains K_p, K_i and K_d are adaptively tuned via a fuzzy inference system (FIS), and the resulting control law can be expressed as:

$$u(k) = K_p(k)e(k) + K_i(k)\sum_{i=0}^{k}e(i) + K_d(k)\frac{de(k)}{dt} \tag{32}$$

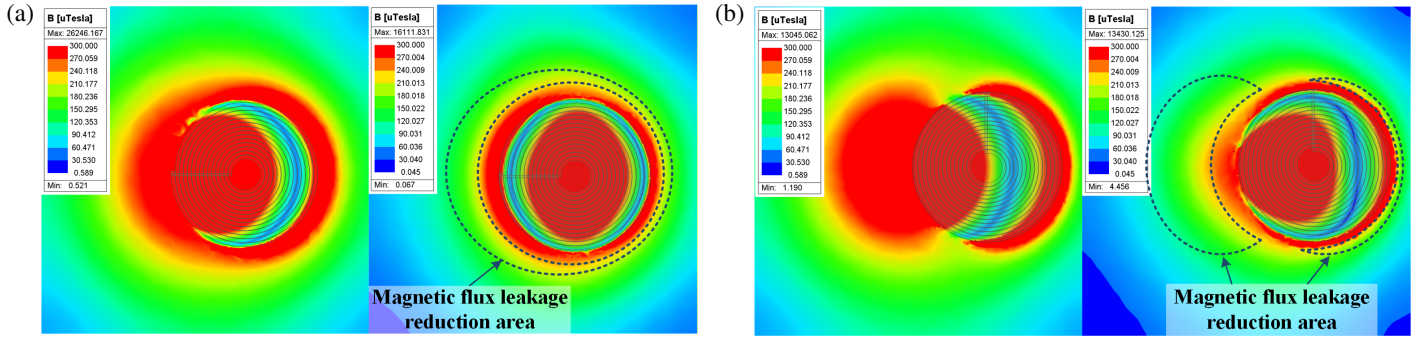

FIGURE 14. Magnetic flux density distributions under different misalignments. (a) Magnetic field distribution at x-axis offsets of 15 mm. (b) Magnetic field distribution at $x = 30$ mm.

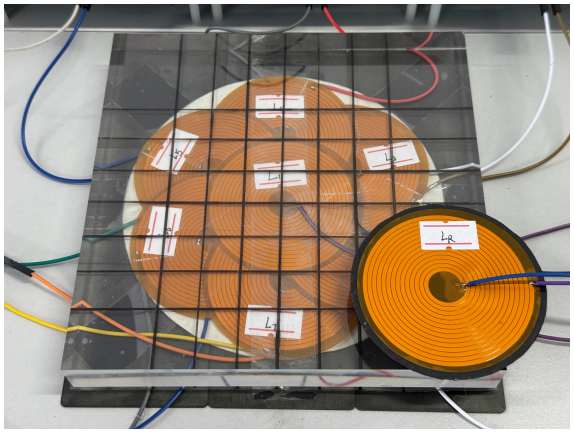

FIGURE 15. Experimental model of the proposed coupling mechanism.

The initial gains K_{p0}, K_{i0}, K_{d0} are tuned based on the linearized system model, while the incremental terms K_p, K_i, K_d are updated online by the fuzzy inference system. Both input and output variables are partitioned into five fuzzy subsets-NB (negative big), NS (negative small), ZO (zero), PS (positive small), and PB (positive big)-with symmetric triangular membership functions to ensure smooth parameter transitions. The fuzzy rules are designed as follows: when the error e is large (in the PB or NB regions), the proportional gain K_p is increased to enhance the dynamic response, whereas the integral gain K_i is reduced to prevent integral windup. When the error rate e_c is large, the derivative gain K_d is appropriately increased to suppress rapid voltage fluctuations and overshoot. As the system approaches steady state, K_p and K_d are gradually decreased while K_i is increased, thereby improving steady-state accuracy and enabling smooth convergence. Through this rule-based adaptive tuning, the proposed controller maintains efficient and stable power transfer performance under variations in coupling coefficient or load conditions.

4.5. Comparative Evaluation of Magnetic Field Distribution and Power Transfer Stability

Following the validation of the position prediction method, it is combined with the multi-transmitter coil excitation strategy and compared with the scheme reported in [35], which uses a large transmitter coil to cover the entire charging area, to evaluate performance differences in implantable wireless power transfer. Accordingly, a single-coil model is established based on the parameters in Table 5 (with the receiving coil kept identical), and finite-element simulations are performed to analyze the magnetic field distribution and leakage characteristics of both configurations under various lateral misalignment conditions.

TABLE 5. Shape parameters of a single large coil.

Thickness (mm)	Outer Diameter (cm)	Turn Pitch (mm)	Trace Width (mm)	Number of Turns	Inner Diameter (mm)
0.035	12	0.21	1.47	28	25.92

Two typical scenarios with lateral offsets of 15 mm and 30 mm along the x-axis are selected for comparison, and the corresponding magnetic field distributions are shown in Figure 14. The results indicate that a large transmitter coil structure can extend the transmission distance and improve alignment tolerance, but the magnetic flux distribution is relatively dispersed, leading to stronger leakage fields and potential electromagnetic exposure risks. In contrast, the proposed MTSR-WPT system achieves local magnetic field confinement through sectional excitation, maintaining high coupling strength while significantly suppressing far-field leakage. Furthermore, using the same efficiency derivation method as for the MTSR-WPT system, its mechanism can be analyzed as expressed in Equation (33):

$$\eta_{single} = \left(1 + \frac{R_{Tx}\frac{|Z_{Rx}|^2}{\omega^2 M^2} + R_{Rx}}{\alpha R_L}\right)^{-1} \tag{33}$$

It can be observed that as lateral misalignment increases, the mutual inductance M of the single-coil system drops rapidly, causing the term $(R_{Tx}|Z_{Rx}|^2)/(\omega^2 M^2)$ to increase significantly and the transmission efficiency to decrease. Maintaining the output then requires higher excitation current, which in turn increases leakage fields. In contrast, the proposed MTSR-WPT system activates only 1–4 sub-coils near the receiver, keeping

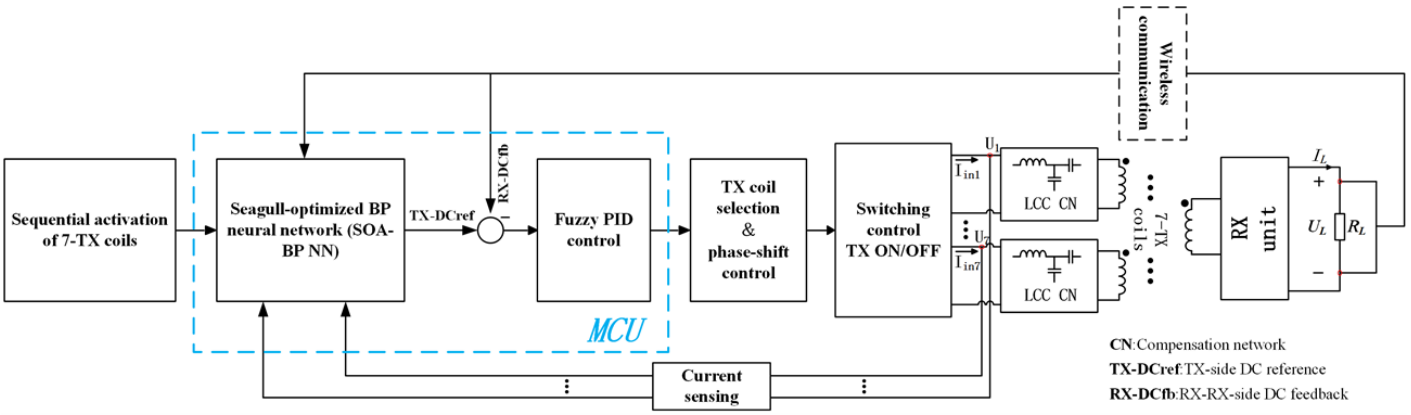

FIGURE 16. Control logic diagram of the MTSR-WPT system.

the equivalent mutual inductance M_{eq} relatively high at offset positions. Meanwhile, copper losses increase linearly, and the EDR is substantially reduced, resulting in superior efficiency and safety compared with the single-coil system. This represents a key advantage for implantable medical applications.

This behavior can be further explained from the perspective of magnetic flux superposition. When a subset of the transmitting units in the array is selectively activated, the total magnetic flux density at the receiver can be expressed as the vector summation of the magnetic fields generated by the individual coils [36]:

$$B_{tot}(r) = \sum_{i=1}^{n} B_i(r) \tag{34}$$

Here, $B_i(r)$ denotes the magnetic field at point r generated by the ith Tx coil, which is proportional to its current $I_{Tx,i}e^{j\phi_i}$. Accordingly, the system's effective mutual inductance can be defined as:

$$M_{\text{eq}}(\mathcal{A}) = \frac{1}{\sum_{i=1}^{N} I_{Tx,i}e^{j\phi_i}} \int_{S_R} B_{\text{tot}}(r)\, dS \tag{35}$$

Equation (35) shows that M_{eq} depends on the superposed Tx magnetic fields over the receiver area S_R, weighted by current amplitudes and phases. By activating only Tx units near the Rx, the system locally reinforces the magnetic field, enabling dynamic field reconfiguration. When the Rx shifts, neighboring coils are activated to maintain continuous coverage and prevent abrupt mutual inductance drop. Compared to a single-coil system, this approach stabilizes coupling and ensures safer, more reliable wireless power for implantable medical devices.

5. EXPERIMENTAL VERIFICATION

To validate the proposed FPCB-based small-coil-array MTSR-WPT system and the position-prediction-based adaptive excitation strategy, an experimental platform is established, and key performance metrics are evaluated. The overall control architecture is shown in Figure 16. Seven transmitting units are sequentially activated for initial excitation, after which an SOA-BP neural network combined with a fuzzy PID controller performs receiver position estimation and adaptive voltage regulation. The resulting control signals drive transmitter selection and phase-shift modulation to achieve accurate target-coil excitation. The control logic is implemented using two cooperative MCUs, enabling efficient and robust wireless power transfer under misalignment conditions.

Based on the above system framework, an experimental platform is constructed as shown in Figure 17. The system mainly consists of MCUs, a DC power supply, transmitter circuits, a coupling structure, receiver circuits, and an electronic load. The coupling structure, shown in Figure 15, is fabricated from FPCB using polyimide (PI) as the insulating substrate.

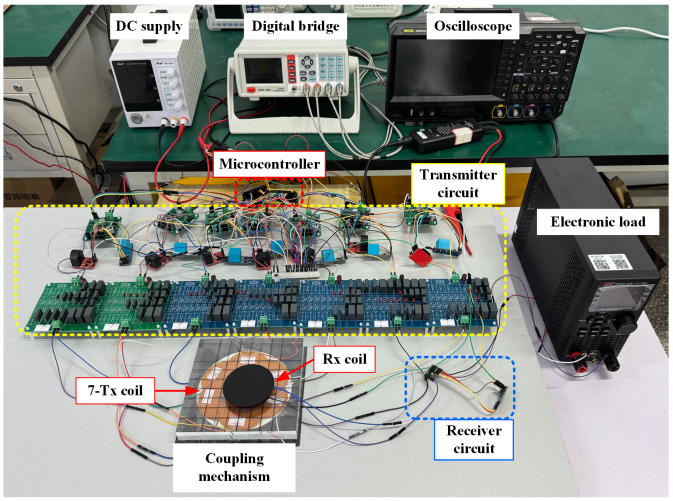

FIGURE 17. Main parameters of the experimental platform.

The control system employs two ESP32-S3-N16R8 microcontrollers: one runs the SOA-BP neural network model for receiver coil position detection, while the other executes a fuzzy PID algorithm for output voltage regulation. Both collaborate in controlling the switches of the transmitter units and communicate wirelessly via the ESP-NOW protocol.

At the receiver, an MB10S-50MIL bridge rectifier converts AC signals, and an RK8510C electronic load provides constant-resistance testing. Output voltage and current are measured

TABLE 6. System parameters.

Parameter	Name	Value	Parameter	Name	Value
U_s (V)	Supply Voltage	12	$C7$ (nF)	Series Compensation Capacitor of Coil 4	279.3
f (kHz)	Operating Frequency	100	$C9$ (nF)	Series Compensation Capacitor of Coil 5	271.9
R_L (Ω)	Load Resistance	10	$C11$ (nF)	Series Compensation Capacitor of Coil 6	279.4
C_L (μF)	Filter Capacitance	100	$C13$ (nF)	Series Compensation Capacitor of Coil 7	274.5
$L11$ (μH)	Inductance of Coil 1	10.61	$C2$ (nF)	Parallel Compensation Capacitor of Coil 1	1361.8
$L12$ (μH)	Inductance of Coil 2	11.35	$C4$ (nF)	Parallel Compensation Capacitor of Coil 2	1347.4
$L13$ (μH)	Inductance of Coil 3	11.24	$C6$ (nF)	Parallel Compensation Capacitor of Coil 3	1340.3
$L14$ (μH)	Inductance of Coil 4	10.95	$C8$ (nF)	Parallel Compensation Capacitor of Coil 4	1347.6
$L15$ (μH)	Inductance of Coil 5	11.14	$C10$ (nF)	Parallel Compensation Capacitor of Coil 5	1391.8
$L16$ (μH)	Inductance of Coil 6	10.97	$C12$ (nF)	Parallel Compensation Capacitor of Coil 6	1319.4
$L17$ (μH)	Inductance of Coil 7	11.14	$C14$ (nF)	Parallel Compensation Capacitor of Coil 7	1333.6
$C1$ (nF)	Series Compensation Capacitor of Coil 1	289.8	$L2$ (μH)	Inductance of Receiver Coil	11.52
$C3$ (nF)	Series Compensation Capacitor of Coil 2	267.1	$C15$ (nF)	Compensation Capacitor of Receiver Coil	219.4
$C5$ (nF)	Series Compensation Capacitor of Coil 3	270.9			

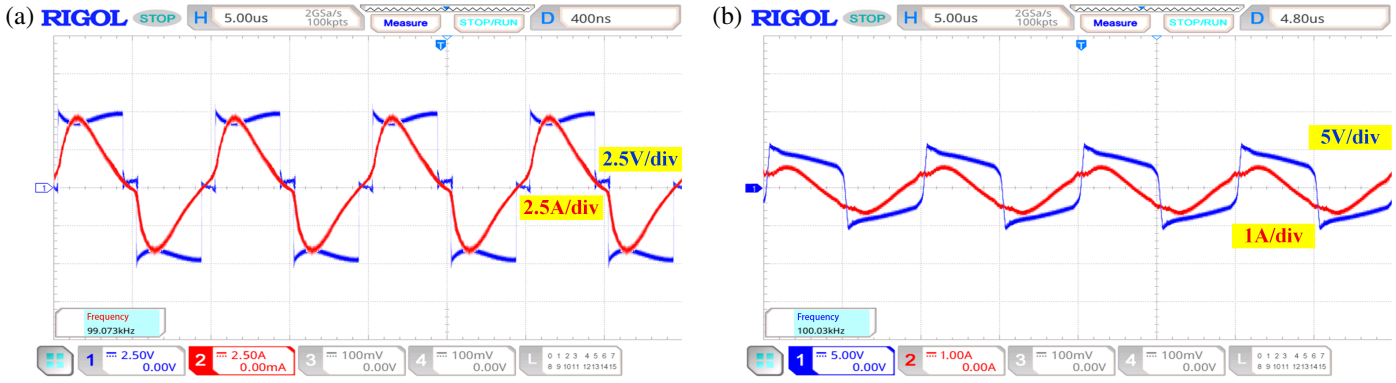

FIGURE 18. Output waveforms at zero x-axis offset: (a) Transmitter-side current and voltage; (b) Receiver-side current and voltage.

using a RIGOL MSO5104 oscilloscope and RP1001C current probe, respectively. A VICTOR 4090C digital LCR meter is used to measure key parameters of the coupling structure. The main system parameters are listed in Table 6.

As illustrated in Figure 18(a), when the receiving coil is located in Region 1 and only the central transmitting unit activated, the rms value of the transmitter current is 3.41 A, representing a reduction of approximately 38% compared with the 5.52 A required by a large single-coil transmitter. Meanwhile, the equivalent series resistance of the large coil is 2.765 Ω, whereas that of the small coil is only 0.725 Ω, indicating a substantial advantage in copper loss. Therefore, employing a size-matched FPCB-based small-coil array effectively reduces transmission losses and improves overall system efficiency.

Figure 18(b) presents the rectifier input waveform at the receiver under single-coil activation. The current effective value is 0.37 A, the output voltage effective value is 5.012 V, and the total transmitted power is 1.52 W. At a coupling distance of 20 mm, the DC-DC conversion efficiency is 9.2%.

As shown in Figure 19, when the receiving coil is located in Regions 2 and 3, the input current of the transmitter-side compensation network exhibits different distribution characteristics. When all four transmitting units are simultaneously activated, the total rms current reaches 8.103 A, which is consistent with the reference result obtained using a single large coil. The equivalent series resistances of the four transmitting coils are 0.642 Ω, 0.672 Ω, 0.768 Ω, and 0.714 Ω, respectively. Owing to the absence of an impedance-matching network and the dissipation of part of the power in the driving and control modules, the overall DC-DC efficiency decreases to 6.2%. As the number of activated coils increases, the energy transfer paths become more complex, leading to additional losses. Further analysis indicates that when the receiving coil moves along the x-axis into Region 3 and triggers three-coil activation, the transmitter current increases markedly, suggesting that an uneven power distribution can induce current surges. Therefore, in practical designs, increased copper thickness is recommended to suppress thermal rise and prevent structural degradation.

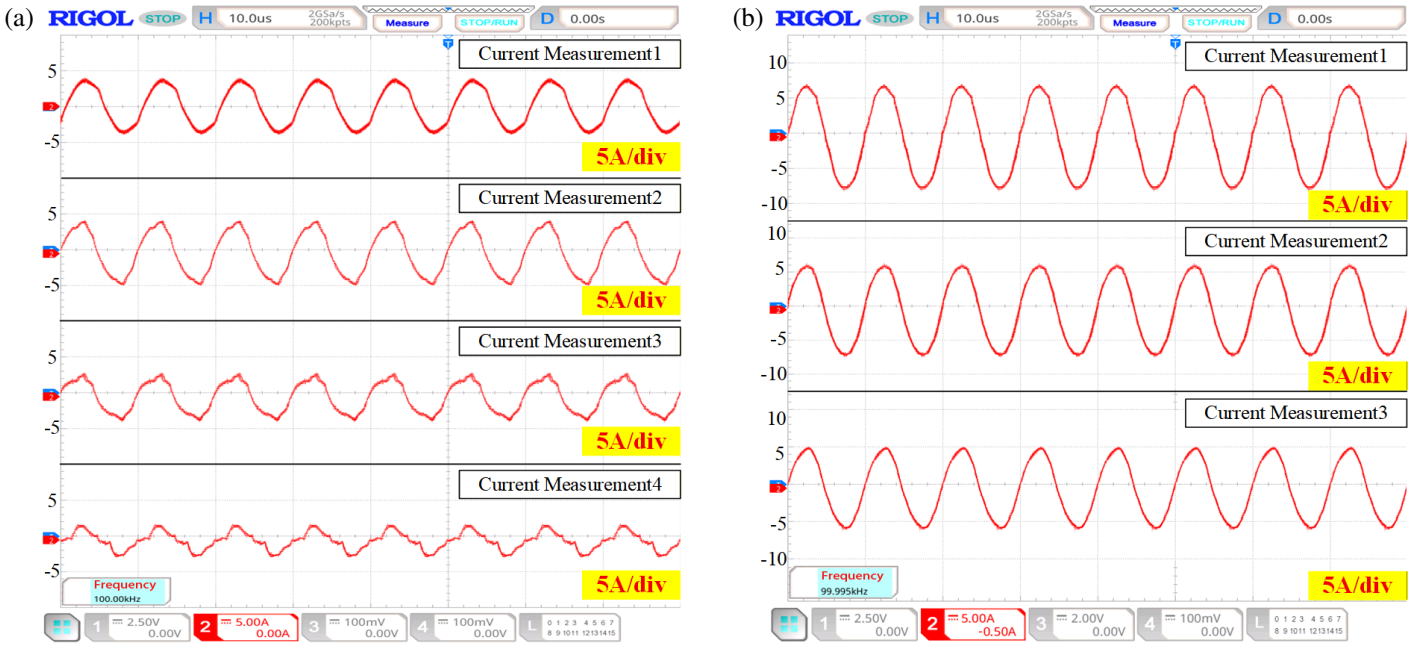

FIGURE 19. Waveform diagram of current output at the transmitter. (a) X-axis displacement: 15 mm, (b) X-axis displacement: 30 mm.

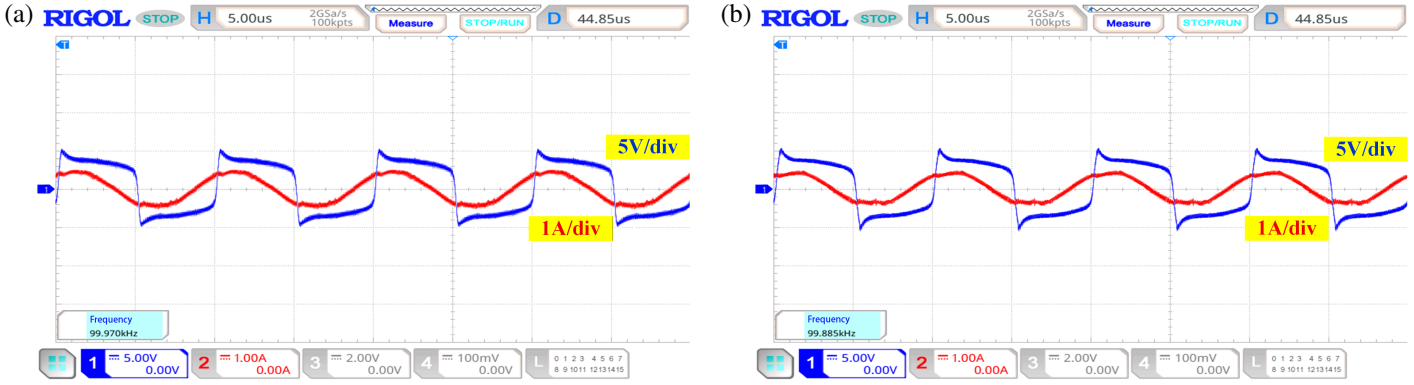

FIGURE 20. Waveform diagram of current and voltage output at the receivier (a) X-axis displacement: 15 mm, (b) X-axis displacement: 30 mm.

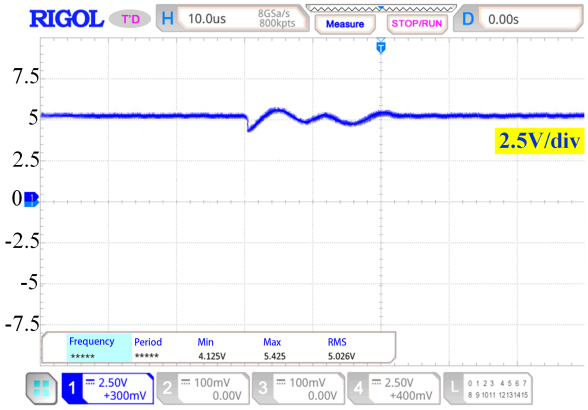

FIGURE 21. Experimental results of output voltage at the moment of launch unit switching.

Figure 20 presents the input waveforms of the receiver-side rectifier under four-coil and three-coil activation conditions, respectively. The results show that the rms values of both voltage and current are nearly identical to those obtained under single-coil activation, confirming that the fuzzy PID controller effectively stabilizes the output voltage through phase-angle regulation. Consequently, the proposed system maintains robust and stable operation under both multi-transmitter switching and steady-state conditions in the MTSR-WPT configuration.

The load-end voltage output is shown in Figure 21. It can be observed that at the moment of transmitter unit switching, the output voltage at the receiving end drops suddenly from a steady state of approximately 5.0 V to about 4.1 V, and then recovers to the steady state after approximately two cycles of decaying oscillations. This transient is caused by the sudden change in the transmitting end's equivalent impedance $Z_{Tx,i}$ and equivalent mutual inductance M_{eq} during switching (see

Equations (4)–(7) and (9)), leading to an instantaneous redistribution of the transmitting and receiving currents. At the same time, the LCC-S compensation loop and the energy storage elements of the coil generate free oscillations during the energy redistribution process, with the damping determined by the system's resistance. Eventually, the system returns to the target voltage level after the controller reestablishes the new steady-state conditions. This demonstrates that the multi-coil coupling model designed in this paper is capable of maintaining relatively stable output power even under offset conditions.

6. CONCLUSION

This paper addresses the efficiency and safety challenges of WPT systems for implantable medical devices by proposing and validating a FPCB-based MTSR-WPT system. A theoretical model is developed to analyze the constraints of the coupling coefficient and quality factor on transmission efficiency, which guides the optimization of coil structures. Using finite-element simulations and equivalent circuit analysis, an array topology with sectional excitation is designed to concentrate the magnetic field under two-dimensional misalignment while effectively suppressing far-field leakage. To tackle mutual inductance nonlinearity and position uncertainty, a SOA-BP is employed for receiver coil position prediction, coupled with fuzzy PID control for adaptive voltage regulation, ensuring robust and stable operation under misalignment and disturbances. The experimental results demonstrate that the proposed system maintains flexibility while significantly enhancing the power transfer efficiency and reducing the leakage fields. Future work will focus on improving the FPCB array fabrication for miniaturization and integration, optimizing the excitation current distribution in the transmitter array, and extending the system to biomedical simulation environments in compliance with IEC/IEEE. This will enable systematic analysis of electromagnetic exposure, tissue heating, and SAR under various power conditions, providing a foundation for the development of clinically viable wireless power systems.

REFERENCES

[1] Ben Amar, A., A. B. Kouki, and H. Cao, "Power approaches for implantable medical devices," *Sensors*, Vol. 15, No. 11, 28 889–28 914, 2015.

[2] Essa, A., E. Almajali, S. Mahmoud, R. E. Amaya, S. S. Alja'Afreh, and M. Ikram, "Wireless power transfer for implantable medical devices: Impact of implantable antennas on energy harvesting," *IEEE Open Journal of Antennas and Propagation*, Vol. 5, No. 3, 739–758, 2024.

[3] Shah, I. A., M. Zada, S. A. A. Shah, A. Basir, and H. Yoo, "Flexible metasurface-coupled efficient wireless power transfer system for implantable devices," *IEEE Transactions on Microwave Theory and Techniques*, Vol. 72, No. 4, 2534–2547, 2024.

[4] Faisal, F., M. Zada, H. Yoo, I. B. Mabrouk, M. Chaker, and T. Djerafi, "An ultra-miniaturized antenna with ultra-wide bandwidth for future cardiac leadless pacemaker," *IEEE Transactions on Antennas and Propagation*, Vol. 70, No. 7, 5923–5928, 2022.

[5] Corva, D. M., B. Parke, A. West, E. H. Doeven, S. D. Adams, S. J. Tye, P. Hashemi, M. Berk, and A. Z. Kouzani, "Smartstim: An artificial intelligence enabled deep brain stimulation device," *IEEE Transactions on Medical Robotics and Bionics*, Vol. 6, No. 2, 674–684, 2024.

[6] Yip, M., R. Jin, H. H. Nakajima, K. M. Stankovic, and A. P. Chandrakasan, "A fully-implantable cochlear implant soc with piezoelectric middle-ear sensor and arbitrary waveform neural stimulation," *IEEE Journal of Solid-State Circuits*, Vol. 50, No. 1, 214–229, 2015.

[7] Na, K., H. Jang, H. Ma, and F. Bien, "Tracking optimal efficiency of magnetic resonance wireless power transfer system for biomedical capsule endoscopy," *IEEE Transactions on Microwave Theory and Techniques*, Vol. 63, No. 1, 295–304, 2015.

[8] Jang, J., I. Habibagahi, H. Rahmani, and A. Babakhani, "Wirelessly powered, batteryless closed-loop biopotential recording IC for implantable leadless cardiac monitoring applications," in *2021 IEEE Biomedical Circuits and Systems Conference (BioCAS)*, 1–4, Berlin, Germany, October 2021.

[9] Piech, D. K., B. C. Johnson, K. Shen, M. M. Ghanbari, K. Y. Li, R. M. Neely, J. E. Kay, J. M. Carmena, M. M. Maharbiz, and R. Muller, "A wireless millimetre-scale implantable neural stimulator with ultrasonically powered bidirectional communication," *Nature Biomedical Engineering*, Vol. 4, No. 2, 207–222, 2020.

[10] Jeong, S., J. Song, S. Lee, S. Hong, B. Sim, H. Kim, S. Kim, and J. Kim, "Design, simulation and measurement of flexible PCB coils for wearable device wireless power transfer," in *2018 IEEE Wireless Power Transfer Conference (WPTC)*, 1–4, Montreal, QC, Canada, Jun. 2018.

[11] Zhao, L., X. Chen, J. Xiao, V. Cirimele, H. Hu, and P. A. Hu, "A high power density and nearly constant voltage WPT system based on bendable PCB," *IEEE Transactions on Industrial Electronics*, Vol. 72, No. 12, 14 931–14 936, 2025.

[12] Zhao, Y., S. Shen, F. Yin, and L. Wang, "A high misalignment-tolerant hybrid coupler for unmanned aerial vehicle WPT charging systems," *IEEE Transactions on Transportation Electrification*, Vol. 11, No. 1, 1570–1581, 2025.

[13] Liu, D., H. Hu, and S. V. Georgakopoulos, "Misalignment sensitivity of strongly coupled wireless power transfer systems," *IEEE Transactions on Power Electronics*, Vol. 32, No. 7, 5509–5519, 2017.

[14] Li, Y., J. Zhao, Q. Yang, L. Liu, J. Ma, and X. Zhang, "A novel coil with high misalignment tolerance for wireless power transfer," *IEEE Transactions on Magnetics*, Vol. 55, No. 6, 1–4, 2019.

[15] Mi, C. C., G. Buja, S. Y. Choi, and C. T. Rim, "Modern advances in wireless power transfer systems for roadway powered electric vehicles," *IEEE Transactions on Industrial Electronics*, Vol. 63, No. 10, 6533–6545, 2016.

[16] Matsuura, K., M. Ishihara, A. Konishi, K. Umetani, and E. Hiraki, "Multiple-transmitter achieving load-independent transmitter current and compensation of cross-interference among transmitters for wide charging area wireless power transfer systems," in *2020 IEEE Energy Conversion Congress and Exposition (ECCE)*, 5474–5481, Detroit, MI, USA, 2020.

[17] Al Mahmud, S. A., I. Panhwar, and P. Jayathurathnage, "Large-area free-positioning wireless power transfer to movable receivers," *IEEE Transactions on Industrial Electronics*, Vol. 69, No. 12, 12 807–12 816, 2022.

[18] Zhang, W. and C. C. Mi, "Compensation topologies of high-power wireless power transfer systems," *IEEE Transactions on Vehicular Technology*, Vol. 65, No. 6, 4768–4778, 2016.

[19] Steigerwald, R. L., "A comparison of half-bridge resonant converter topologies," *IEEE Transactions on Power Electronics*, Vol. 3, No. 2, 174–182, 1988.

[20] Zeng, Y., D. Qiu, X. Meng, B. Zhang, and S. C. Tang, "Optimized design of coils for wireless power transfer in implanted medical devices," *IEEE Journal of Electromagnetics, RF and Microwaves in Medicine and Biology*, Vol. 2, No. 4, 277–285, 2018.

[21] Abduljaleel, H. K., S. K. Gharghan, and A. J. A. Al-Gburi, "Multi-layer square coil-based wireless power transfer for biomedical implants," *Progress In Electromagnetics Research B*, Vol. 111, 83–98, 2025.

[22] Xu, Q., Q. Hu, H. Wang, Z.-H. Mao, and M. Sun, "Optimal design of planar spiral coil for uniform magnetic field to wirelessly power position-free targets," *IEEE Transactions on Magnetics*, Vol. 57, No. 2, 1–9, 2021.

[23] Ongayo, D. and M. Hanif, "Comparison of circular and rectangular coil transformer parameters for wireless power transfer based on finite element analysis," in *2015 IEEE 13th Brazilian Power Electronics Conference and 1st Southern Power Electronics Conference (COBEP/SPEC)*, 1–6, Fortaleza, Brazil, 2015.

[24] Jeong, S., T.-W. Kim, S. Lee, B. Sim, H. Park, K. Son, K. Son, S. Kim, T. Shin, Y.-C. Kim, J. Kim, and B.-J. Kim, "Analysis of repetitive bending on flexible wireless power transfer (WPT) PCB coils for flexible wearable devices," *IEEE Transactions on Components, Packaging and Manufacturing Technology*, Vol. 12, No. 11, 1748–1756, 2022.

[25] Cai, C., S. Wu, Z. Zhang, L. Jiang, and S. Yang, "Development of a fit-to-surface and lightweight magnetic coupler for autonomous underwater vehicle wireless charging systems," *IEEE Transactions on Power Electronics*, Vol. 36, No. 9, 9927–9940, 2021.

[26] Costanzo, A., F. Apollonio, P. Baccarelli, M. Barbiroli, F. Benassi, F. Apollonio, P. Burghignoli, M. Barbiroli, F. Benassi, M. Bozzi, P. Burghignoli, T. Campi, S. Cruciani, S. di Meo, M. Feliziani, W. Fuscaldo, A. Galli, M. Liberti, F. Maradei, P. Marracino, D. Masotti, G. Paolini, M. Pasian, L. Perregrini, G. Schettini, and L. Silvestri, "Wireless power transfer for wearable and implantable devices: A review focusing on the WPT4WID research project of national relevance," in *2021 XXXIVth General Assembly and Scientific Symposium of the International Union of Radio Science (URSI GASS)*, 1–4, Rome, Italy, Oct. 2021.

[27] Yang, C.-L., C.-K. Chang, S.-Y. Lee, S.-J. Chang, and L.-Y. Chiou, "Efficient four-coil wireless power transfer for deep brain stimulation," *IEEE Transactions on Microwave Theory and Techniques*, Vol. 65, No. 7, 2496–2507, 2017.

[28] Yan, X., J. Yao, W. Chen, and Y. Song, "Wireless power transfer system for cardiac pacemakers based on multi-coil series magnetic integration," *Progress In Electromagnetics Research C*, Vol. 143, 87–98, 2024.

[29] Li, D., X. Wu, W. Gao, and J. Gao, "Multi-mode joint modulation of array wireless power transfer," *Scientific Reports*, Vol. 13, No. 1, 15780, 2023.

[30] Wang, W., Z. Yu, Y. Zou, J. E. Woods, P. Chari, Y. Su, J. T. Robinson, and K. Yang, "Omnidirectional wireless power transfer for millimetric magnetoelectric biomedical implants," *IEEE Journal of Solid-State Circuits*, Vol. 59, No. 11, 3599–3611, 2024.

[31] Huh, S., B. Park, S. Choi, Y. Shin, H. Kim, J. Kim, J. Park, D. Park, and S. Ahn, "Transmitter coils selection method for wireless power transfer system with multiple transmitter coils and single receiver coil," *IEEE Transactions on Power Electronics*, Vol. 38, No. 3, 4092–4109, 2023.

[32] Gao, Y., C. Duan, A. A. Oliveira, A. Ginart, K. B. Farley, and Z. T. H. Tse, "3-D coil positioning based on magnetic sensing for wireless EV charging," *IEEE Transactions on Transportation Electrification*, Vol. 3, No. 3, 578–588, 2017.

[33] Fu, Y., H. Tang, J. Luo, and Z. Peng, "Anti-offset multicoil underwater wireless power transfer based on a BP neural network," *Machines*, Vol. 12, No. 4, 275, 2024.

[34] Li, H.-X., L. Zhang, K.-Y. Cai, and G. Chen, "An improved robust fuzzy-PID controller with optimal fuzzy reasoning," *IEEE Transactions on Systems, Man, and Cybernetics, Part B (Cybernetics)*, Vol. 35, No. 6, 1283–1294, 2005.

[35] Machnoor, M., E. S. G. Rodríguez, P. Kosta, J. Stang, and G. Lazzi, "Analysis and design of a 3-coil wireless power transmission system for biomedical applications," *IEEE Transactions on Antennas and Propagation*, Vol. 67, No. 8, 5012–5024, 2019.

[36] Kiani, M. and M. Ghovanloo, "The circuit theory behind coupled-mode magnetic resonance-based wireless power transmission," *IEEE Transactions on Circuits and Systems I: Regular Papers*, Vol. 59, No. 9, 2065–2074, 2012.